Tissue-Like Multicellular Development Triggered by Mechanical Compression in Archaea

Theopi Rados[1]†, Olivia S. Leland[1]†, Pedro Escudeiro[2], John Mallon[1], Katherine Andre[1], Ido Caspy[3], Andriko von Kügelgen[3] Elad Stolovicki[4], Sinead Nguyen[1], Inés Lucía Patop[1], Thiberio Rangel[5], Sebastian Kadener[1], Lars D. Renner[6], Vera Thiel[7], Yoav Soen[4], Tanmay A.M. Bharat[3], Vikram Alva[2], Alex Bisson[1]*

[1]Brandeis University, Department of Biology; Waltham, MA, USA

[2]Department of Protein Evolution, Max Planck Institute for Biology Tübingen; Tübingen 72076, Germany

[3]Structural Studies Division, MRC Laboratory of Molecular Biology; Cambridge, United Kingdom

[4]Department of Biomolecular Sciences, Weizmann Institute of Science; Israel

[5]Department of Earth, Atmospheric, & Planetary Sciences, Massachusetts Institute of Technology; Cambridge, MA, USA

[6]Leibniz Institute of Polymer Research and the Max Bergmann Center of Biomaterials; Dresden, Germany

[7]Department of Microorganisms, Leibniz Institute DSMZ – German Collection of Microorganisms and Cell Cultures GmbH; Germany

† These authors contributed equally to this work and share the first authorship

* Correspondence should be addressed to bisson@brandeis.edu

Abstract

The advent of clonal multicellularity is a critical evolutionary milestone, seen often in eukaryotes, rarely in bacteria, and only once in archaea. We show that uniaxial compression induces clonal multicellularity in haloarchaea, forming tissue-like structures. These archaeal tissues are mechanically and molecularly distinct from their unicellular lifestyle, mimicking several eukaryotic features. Notably, archaeal tissues undergo a coenocytic stage followed by a tubulin-independent cellularization, orchestrated by active membrane tension at a critical cell size. Past cellularization, tissues are organized into two cell types - apical and basal scutoids - with junction elasticity akin to animal tissues, with actin and protein glycosylation as fiducial polarity markers. Our findings highlight the remarkable biophysical potential of convergent evolution in the emergence of multicellular systems across domains of life.

Main Text

The definition of multicellularity is as controversial as the diversity of organisms capable of clonal (related to one genetic lineage) or aggregative (cluster of multiple organisms) multicellularity (*1*). Although the evolutionary pressures leading to multicellular lifestyle remain unclear, experimental evolution suggests that selection favors increased size, mechanical strength, and the differentiation of cells into specialized functions (*2–5*). Once mistaken for bacteria due to their lack of nuclei, archaea are now recognized as forming a monophyletic group with eukaryotes (*6*). At the cellular level, most archaea lack a rigid cell wall and are encapsulated by a proteinaceous surface (S-layer), a 2D paracrystalline lattice comprised of glycoproteins (*7*, *8*). While this cellular envelope makes archaea mechanically vulnerable, it facilitates close interactions between cells, such as cell-cell contact and fusion, which may have played a role in the emergence of eukaryotes (*9*, *10*). However, the evolution of mechanosensory responses driven by the lack of rigid cell wall remains elusive. The unique combination of genetic and biophysical traits prompted us to investigate the mechanobiology of archaeal cells, leading to the serendipitous discovery of a reversible, clonal developmental tissue-like multicellular program.

Uniaxial compression gives rise to clonal, tissue-like multicellularity

To gain insights into the mechanobiology of archaeal cells, we performed confinement experiments leveraging straightforward cultivation and genetics of the salt-loving *Haloferax volcanii* (*Hvo*) (*11*). First, we established a baseline for unperturbed haloarchaeal cells trapped within a custom microfluidic device (Fig. 1A and S1A). Cells growing within microfluidic traps showed cell morphologies comparable to those in bulk liquid cultures, suggesting that cells were not mechanically stressed (Fig. 1C and S1B; Movie S1). Next, we imaged cells under agarose pads, a standard technique for microbial immobilization (Fig. 1B). Unlike in microfluidics, cells under pads deformed within a single generation (~2.5 hours) at the lowest agarose concentrations, indicating that pad immobilization is incompatible with haloarchaeal imaging for longer periods (Fig. S1B). To quantify the compressive forces involved in deforming cells, we measured the uniaxial forces applied to cells by pads using dynamic mechanical analysis (DMA) (*12*). The storage moduli of 0.25-3.5% pads showed that compression of approximately 1-10 kPa is sufficient to deform *Hvo* cells (Fig. S1C). These values are comparable to the mechanical resistance of eukaryotic cells such as amoeba and mammalian cells but orders of magnitude lower than most cell-walled organisms (*13*, *14*).

Given the mechanical sensitivity of haloarchaeal cells under pads, we tested the responses of cells under compressive forces above 100 kPa, closer to their natural habitat, such as the human gut and salt plates (*15–17*). When compressed by pads with agarose concentrations above 2%, cells stopped dividing but continued to grow. Unexpectedly, after ~12 hours, we observed cellularization, in which multiple simultaneous septation events carved large cells into compartments. Finally, cells developed into an epithelial-like monolayer, forming connected cellular structures akin to the tessellation patterns in leaf tissues (Fig. 1D and E; Movie S2). The observed morphological development before cellularization also resembles the coenocytic phase of the chytrids and chicken embryogenesis, in which cells grow and multiply their nuclei (*18*, *19*). To confirm that these cells are coenocytes, we inquired whether DNA replication progresses during cell division arrest. Time-lapse imaging of cells expressing a fluorescent fusion of the DNA sliding clamp (mNeonGreen-PCNA) showed the continuous replication during development, confirming that cells under compression go through a coenocyte-like phase preceding cellularization (Fig. 1D; Movie S3).

Animal and plant cells often sense and activate biochemical pathways in response to surface curvatures and material properties (*20*, *21*). Thus, we investigated whether multicellular development depends on the pad's stiffness. To decouple stiffness from compression, cells were immobilized under and on top of a 2.5% agarose pad. After 24 hours, tissue-like structures were exclusively observed when cells were grown under the pads (Fig. S1D), suggesting substrate stiffness alone is not sufficient to induce multicellularity. Furthermore, cells compressed by bilayer "cake" pads developed into tissue-like structures when in contact with the 2.5% agarose surface but continued to propagate as unicellular when facing the 0.25% layer (Fig. S1E). Hence, we conclude that both compression and stiffness are required for multicellularity.

To determine if cells within multicellular structures retain S-layer, we subjected archaeal tissues to mechanical shear (Fig. S2A), cryo-fixed cell resuspension, and imaged individual cells by electron cryomicroscopy (cryo-EM) and tomography (cryo-ET) (Fig. S2B). Concomitantly, we imaged live cells using Brilliant Blue, a fluorescent dye that specifically labels S-layer glycoproteins but not the cytoplasmic membrane (Fig. S2C). Both methods consistently showed S-layer between cells, no different from unicells, confirming that archaeal tissues preserve the S-layer in their intercellular spaces (Fig. 1E).

Next, we explored the possibility of tissues being a product of cell compaction. 3-D imaging of tissues and compressed unicells showed extracellular space between most cells, but no visible spaces within tissues (Fig. 1F; Movie S4). To probe physical connectivity, we used laser ablation to wound areas in the center of the tissues. If the cells were physically connected by junction-like structures, we expected a collectively migration towards the center of the injured area. Following ablation, we observed a directional movement of cells toward the wounds in tissues at speeds ($t_{1/2}$=11.8±2.2 minutes) similar to those seen in wounded animal tissues, but not in unicellular populations (Fig. 1G and S2C; Movie S5) (*22*). Given that archaea lack cytoskeleton motors (e.g., myosin), it is unlikely that the directional motion is a

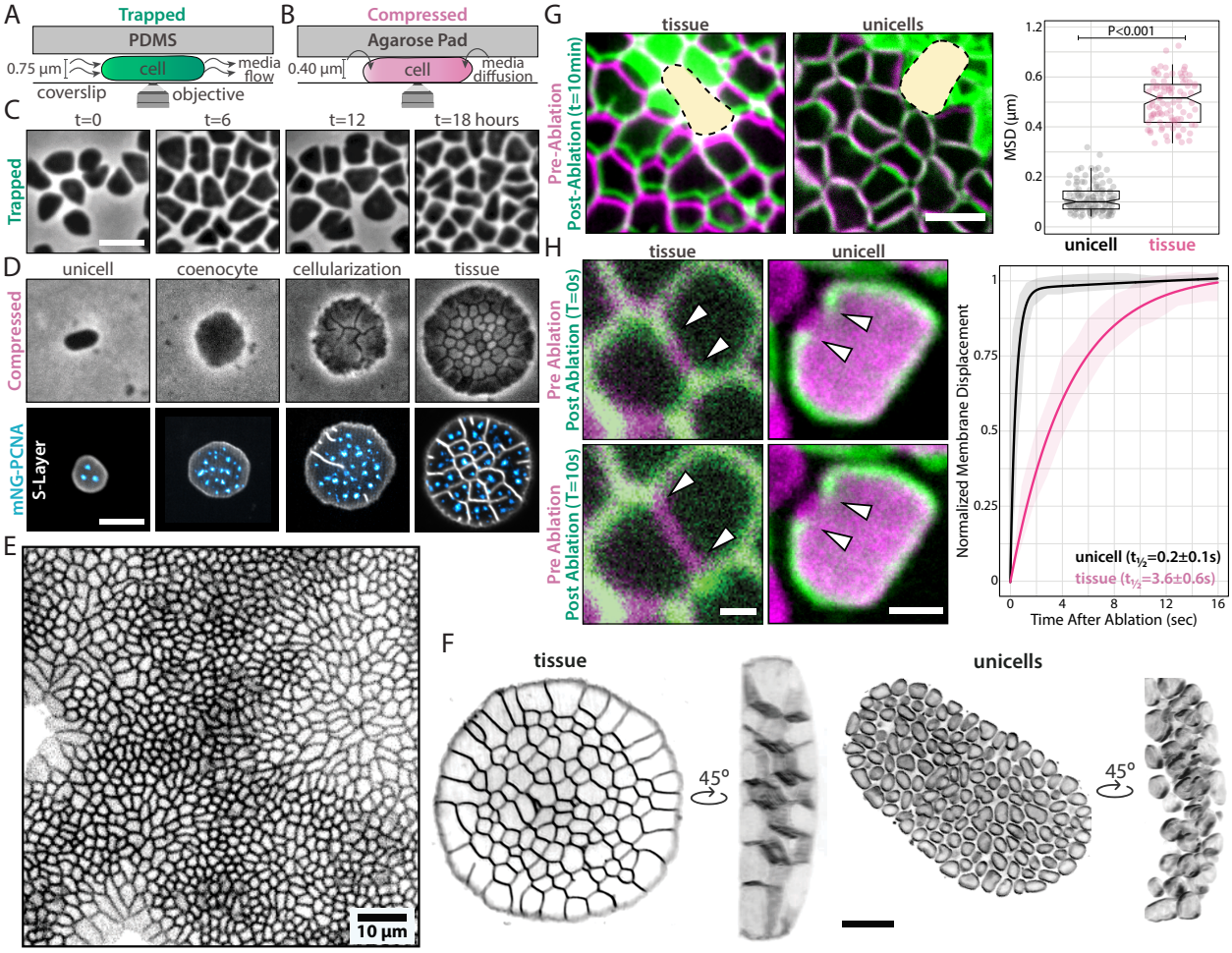

Fig. 1. Uniaxial compression triggers multicellular development in *Hfx. volcani*. Schematic of **(A)** microfluidics and **(B)** agarose pad immobilization. Phase-contrast time-lapses of **(C)** trapped and **(D)** compressed cells across approximately six generations-time where msfGFP-PCNA foci (orange) represent replication sites. **(E)** Stretched and compressed areas comprised in large monolayers of epithelia-like tissues. **(F)** 3D-SoRa microscopy images of a tissue (top) and unicells (bottom) **(G)** Laser ablation of central tissue regions. False-colored overlays of tissues before (magenta) and 10 minutes after (green) ablation. The middle panel represents a zoomed inlet of the top panel. Directional motion from cells was calculated using Mean Square Displacement (MSD). **(H)** Laser ablation of junctions (tissues) and cell membrane (unicells). False-colored overlays of tissues and cells before (magenta) and after (0 and 10 sec, green) ablation. The gap distance between nicked membrane ends was plotted against time, and half-lives were calculated from second-order polynomial curves. The center of the boxplots indicate the median, and the limits of the box define the interquartile range; error bars represent 95% confidence interval (CI). Shaded areas indicate the 95% CI. S-layers were stained with Brilliant Blue. Statistical differences were tested by Kolmogorov-Smirnov. Unless specified, scale bars represent 2 µm.

product of active wound healing as mechanistically described in animal tissues. Instead, it is plausible that both archaeal and animal tissues have similar membrane viscoelastic properties. To test this idea, we measured the retraction rates after ablating a small area of the cell envelope in unicells and the junctional space of archaeal tissues. After severing, we observed a membrane recoil in archaeal tissues like that observed in animal tissues in contrast to a small 1-step retraction from unicells (Fig. 1H; Movie S6). The apparent higher membrane tension in archaeal tissues, associated with faster junction retraction speeds ($t_{1/2}$=3.6±0.6s) compared to compacted unicells ($t_{1/2}$=0.2±0.1s), implies that there are junctional load bearing structures comparable to epithelia (*23*). Ultimately, our results demonstrate that haloarchaea represent a unique class of multicellularity, exhibiting material properties typical of canonical eukaryotic tissues.

Archaeal tissues are widespread in Haloarchaea and counter-correlated with biofilm levels

To understand the evolutionary origins and diversity of haloarchaeal tissues, we created a phylogenomic tree across 57 genera with representatives from all haloarchaeal orders (Data

S1). Based on the resultant clade distributions, we cultivated and imaged compressed cells from 52 species across 14 different genera (Fig. S3). Irrespective of size and growth rate, we found that 61.6% of tested haloarchaeal species formed tissues, with at least one case of tissue development or no multicellularity in every tested genus. Among species that did not form tissue, we identified instances of cell death (Fig. S4A), shape deformation (Fig. S4B), or indifferent to pads (Fig. S4C). Surprisingly, we observed 3 species – *Htg. salina*, *Ncc. jeotgali*, and *Hka. jeotgali* – that exhibit sarcina-like clonal multicellularity similar to *Methanosarcina,* previously the only known multicellular archaeon (Fig. S4D) (*24*). These results suggest that archaeal tissues emerged early in haloarchaeal evolution, remain dominant in the sampled diversity, and have been lost multiple times.

Next, we focused on strains from the *Haloferax* genus, where most species developed tissues (Fig. 2A). However, two species – *Hfx. prahovense* and *Hfx. gibbonsii* – resulted in tissues with unstable junctions (Fig. S5A). Notably, only *Hfx. mediterranei* (*Hmed*) failed to develop tissues, instead growing as stacked cell colonies (Fig. 2B; Movie S7). Although not constituting a monophyletic branch, all three taxa are closely related, with *Hmed* placed on a particularly long branch. We then tested if *Hmed* cells could still form tissues under higher compression under 5% agarose pads. *Hmed* cells grew larger than *Hvo* coenocytes until they ruptured and swarmed outwards (Fig. 2B; Movie S7). Since the swarming-like motion resembles bacterial biofilm-dependent gliding (*25*), we questioned if *Hmed* cells might have evolved a divergent strategy to survive compression. Supporting this hypothesis, the relative biofilm mass levels in *Hmed* were at least twice as high as those in other *Hfx* strains (Fig. S5B). Although it remains undetermined whether *Hmed* carries mutations suppressing the expression but still hosts the molecular machinery required for multicellularity, the diversification of tissue architecture and survival strategies suggests commonly shared multicellularity potential occasional losses across the genus.

Despite sharing many similar "weed-like" traits, *Hmed* is still outcompeted in nature (*26*). To test if *Hmed*'s lack of multicellularity development results in loss of fitness, we compressed cells under microfabricated pillars intercalated with "relief" zones (Fig. 2C). This setup allowed us to observe

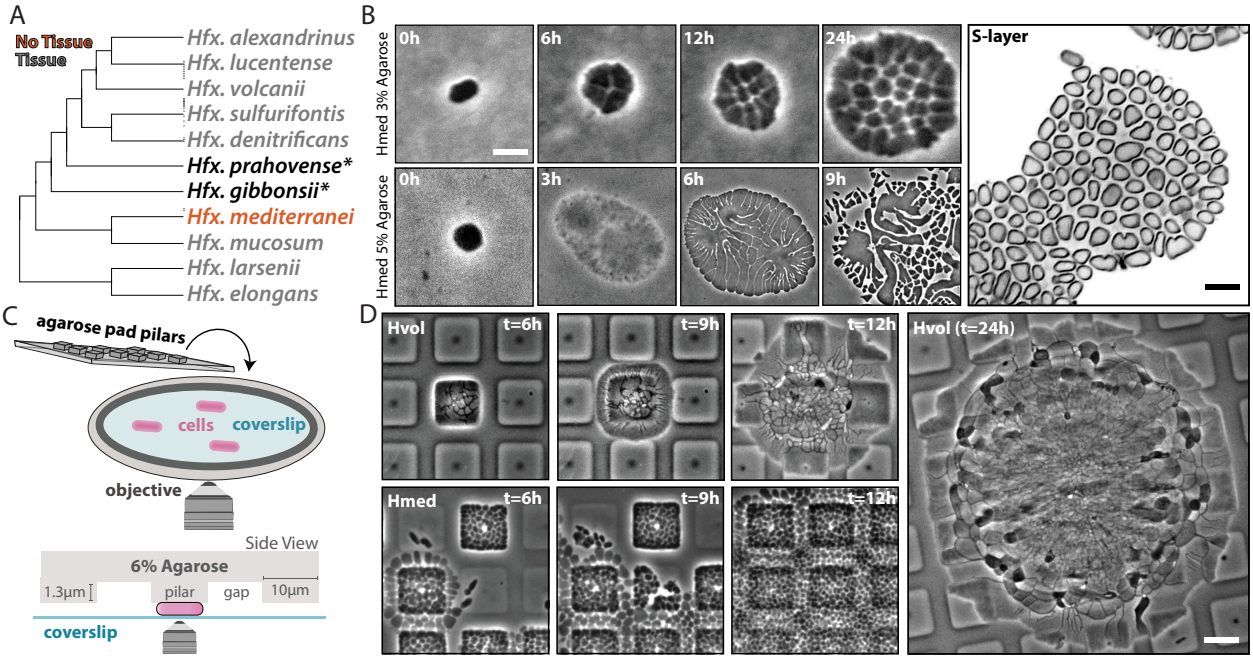

Fig. 2. *Hfx. mediterranei* does not form tissues under compression. (A) Cladogram depicting evolutionary relationships between compressed *Haloferax* species. For comprehensive phylogenetic tree, see Supplementary Data S1. **(B)** Phase-contrast time-lapses (left) of *Hfx. mediterranei* growth under 3% (top) and 5% (bottom) agarose pads. (right) SoRa microscopy of *Hfx. mediterranei* growth after 24 hours under 3% agarose pads. S-layers were stained with Brilliant Blue. **(C)** Cartoon representation of microfabricated pillars used in the intermittent compression experiments. **(D)** (left) Phase-contrast time-lapses of *Hfx. volcanii* (top) and *Hfx. mediterranei* (bottom) under micropillar devices. (right) *Hfx. volcanii* tissues after 24-hour incubation under the micropillar device. Unless specified, scale bars represent 2 µm.

how these cells navigated mechanical "escape room" challenges, mimicking their natural habitat. While *Hvo* cells managed to propagate even with low initial cell numbers, *Hmed* could only spread across larger areas as unicells when inoculated at high numbers (Fig. 2D; Movie S8). Therefore, we propose that mechano-responsive multicellularity was selected in compressive zones exceeding lethal thresholds in haloarchaeal environments, such as desiccated salt plates, animal guts, and microbial biofilms (*27*).

Archaeal tissues have two distinct cell types and undergo FtsZ-independent cellularization

Time-lapses of *Hvo* growing under intermittent uncompressed zones showed tissues with larger peripheral cells (Fig. 2D). Changes in cell size and shape could be a result either from the uneven distribution of mechanical forces in the device or from an underlying mechanosensory mechanism within specific tissue cells. Since the development of specialized cell types is a hallmark of complex multicellularity (*28*), we characterized the morphology and growth in different regions of tissues. 3D micrographs showed two profiles: wider and shorter cells in the periphery, and taller in the center of tissues. As previously mentioned, archaeal tissues resemble the architecture of plant leaf meristems (*29*), so we annotated cells as apical (outer surface) and basal (inner surface) (Fig. 3A). Imaging tissues by 3D-STED microscopy showed that apical cells are not in contact with the surface of pads, and therefore their height is not a direct product of compression (Fig. 3B; Movie S9). In contrast, basal cells are in contact with compression areas despite being taller, implicating they are specifically responding to the mechanical compression and stiffness from pads (Fig. 3C; Movie S9). Moreover, the basal cell shape resembles animal scutoids known to minimize energy, maximize packing, and stabilize curved epithelia during embryogenesis (*30*). This led us to ask if archaeal scutoids maintain a constant surface-to-volume ratio compared to large apical cells. Markedly, apical volumes and surface areas are larger than basal cells. Still, the ratio between surface cell area and volume remains precisely consistent (Fig. 3D).

To expand on the specialization of basal and apical cells, we compared the growth rates and lifespans between apical, basal, and unicells. While mechanically stressed cells are expected to grow slower and become smaller with shorter lifespans (*31*), both apical and basal cells show higher growth rates and similar lifespans compared to unpacked unicells (Fig. 3E). Altogether, the cell cycle measurements above support the conclusion that cell shapes within tissues represent specialized lifestyles that cannot be summarized by simple mechanical and nutritional stresses.

Specialized cell types within animal tissues often adapt components of their cytoskeleton across different mechanical environments. Therefore, we inquired if multicells still performed cytokinesis by the unicellular mechanisms. The tubulin paralogs FtsZ1 and FtsZ2 are required for cell division but not essential in *Hvo* (*32*). Remarkably, Δ*ftsZ1*Δ*ftsZ2* mutants were still capable of cellularization under compression, but cell junctions were askew in "zigzag" tracks (Fig. 3F). These observations parallel some animals and multicellular holozoans, where microtubules are not required for cellularization but impact viability during their multicellular cycle (*33*). To further understand the role of FtsZs during development, we created a functional knock-in FtsZ1-mChartreuse fusion (*34*) (Fig. S6A). While unicells showed continuous Z-rings, coenocytes exhibited scattered FtsZ1 filaments at the top and bottom of the basal region of coenocytes (Fig. 3G). Supporting the observation that cellularization is independent of FtsZs, we did not observe FtsZ1 at the junction furrow (white arrowheads) until tissue maturation (Fig. S6B). Collectively, these observations support a developmental program with sequential, independent stages, each step producing cell types (coenocytes, basal, and apical cells) specialized molecular machineries.

Archaeal tissue cellularization is triggered by envelope tension

Evidence from flies and holozoans suggests that the timing of cellularization correlates with the ratio between the number of nuclei and cell volume (N/C) (*35*). To test if N/C is involved in triggering cellularization in coenocytes, we imaged cells expressing mNeonGreen-PCNA, quantifying the number of replication sites and the fluorescence intensity within replication sites relative to cell area as a proxy for N/C. The expectation was that, for the N/C ratio to reach the critical threshold for cellularization, DNA replication needs to increase at a higher rate than cell area. However, we observed that replication rates are constant relative to cell area (Fig. S7A). We then tested if other markers, such as size, time, and cell volume added,

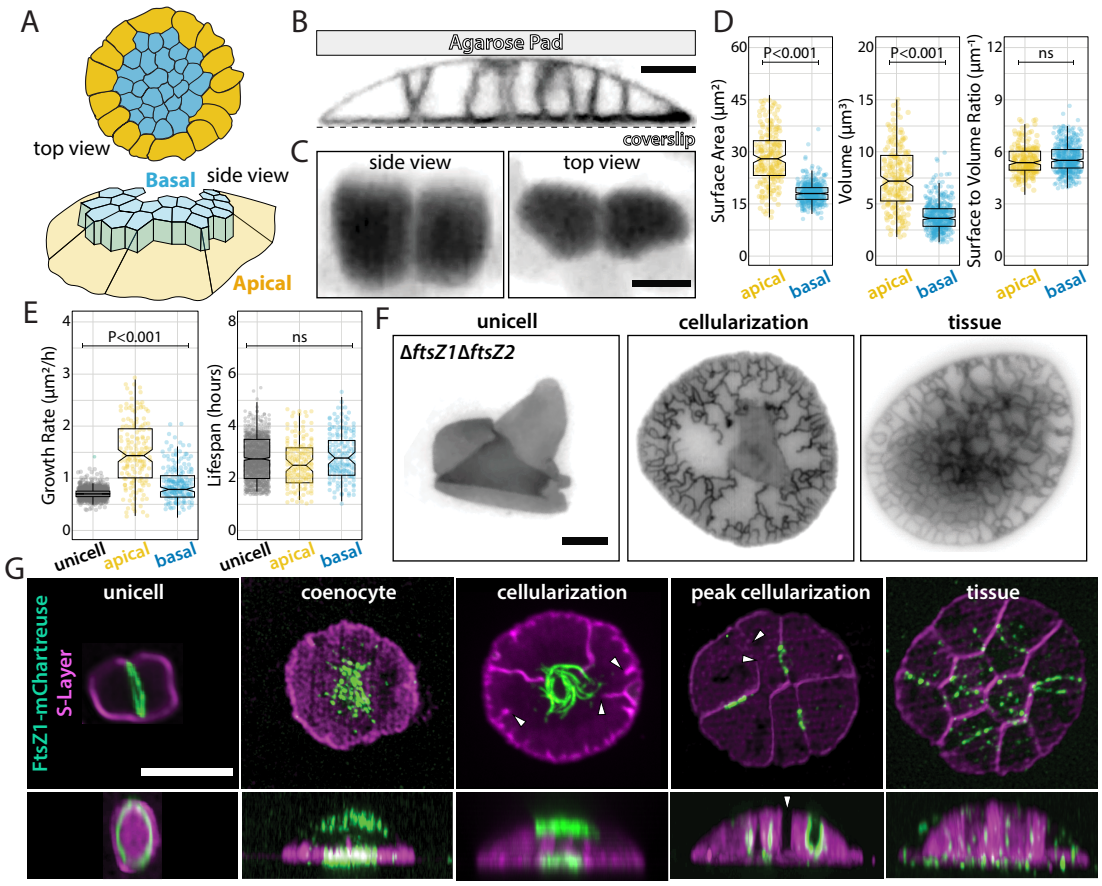

Fig. 3. Cellularization is independent of FtsZs and results in two cell types. (A) Cartoon representation of top and side views showing basal and apical cell types within tissues. **(B)** 3D-STED super-resolution microscopy of cellularization process. **(C)** iSIM of cells expressing cytoplasmic msfGFP highlights basal scutoid cells. **(D)** Surface area and volume measurements of basal and apical cells from 3D projections. (E) Area growth rate and lifespan measurements of unicells, apical, and basal cells from phase-contrast time-lapses. (F) Epifluorescence microscopy of representative cell-division impaired Δ*ftsZ1*Δ*ftsZ2* cells across different developmental stages. Early cellularization represents cells that just entered the cellularization stage. In contrast, peak cellularization represents cells at the onset of completing cellularization (G) 3D-SoRa microscopy of representative cells expressing FtsZ1-mChartreuse across different developmental stages. The center of the boxplots indicate the median, and the box limits define the interquartile range; error bars represent 95% confidence interval (CI). S-layers were stained with Brilliant Blue. Statistical differences were tested by Kolmogorov-Smirnov. Unless specified, scale bars represent 2 µm.

coincide with cellularization (*36*). By tracking these single-cell parameters at cellularization (Fig. 4A and 4B), we observed a lower coefficient of variance for coenocyte area (CV=9.6%) compared to area added and time (CV=24.2% and 47.1%, respectively) (Fig. 4C), suggesting that cellularization happens at a specific coenocyte size. To validate this correlation, we tracked the development of compressed Δ*ftsZ2* cells. Because Δ*ftsZ2* cells do not divide when growing exponentially in liquid cultures, they are larger than control cells and would be expected to cellularize quicker under compression. Indeed, Δ*ftsZ2* cells cellularize approximately 4.2 times faster and added 3.7 times less area but at a similar area threshold to wild type (Fig. 4C).

Although cell size is a consistent parameter at cellularization, the underlying mechanism is unclear. Because of the differences in membrane tension between tissues and unicells (Fig 1H), we hypothesized that cell envelopes accumulate elastic strain as coenocytes become larger, reaching a critical threshold at which cellularization is initiated. To measure the real-time membrane tension in coenocytes, we created bSpoJ, a single-molecule live-cell membrane fluidity reporter. bSpoJ is a chimeric transmembrane domain of SpoIIIJ from *Bacillus subtilis*, with a secretion signal peptide from *Hvo*, and HaloTag. Particle tracking of bSpoJ in *Hvo* showed a 30.3-fold increase in apparent diffusion in coenocytes compared to unicells, an order of magnitude above

the 2.5-fold increase in cell area (Fig. 4D and S7B; Movie S10 and S11).

The disproportional increase in membrane tension relative to cell area suggests that the biochemical composition of the coenocytes is actively changing throughout development. To test this hypothesis, we inquired if perturbing the membrane fluidity as a proxy for tension would affect the cell area at cellularization. As carotenoids have been implied to play a similar role as cholesterol in eukaryotes (*37*), we tested if membrane fluidity would fluctuate in cells unable to produce carotenoids (*car*⁻). As an orthogonal approach to bSpoJ, we measured membrane fluidity in cells stained with Laurdan, a fluorescent probe that intercalates between phospholipids and reports Generalized Polarization (*38*). Despite the lack of obvious phenotypic defects in *car*⁻ unicells at higher or lower temperatures (Fig. S7C), *car*⁻ lack membrane fluidity homeostasis when cultivated at lower temperatures in contrast to wild-type cells (Fig. 4E and S7D). Next, we observed that compressing *car*⁻ cells resulted in a decrease of coenocyte viability (Fig. 4F and S7E). Curiously, the colony pigmentation characteristic of carotenoids seems to be attenuated in *Hmed* and other *Hfx* species that do show defective tissue structures (Fig. S7F and S8). Combined, our results suggest that *car*⁻ membrane homeostasis defects prevent coenocytes to cellularize before critical tension thresholds. As predicted, we observed a shift in cell area at cellularization correlated to *car*⁻ loss of viability at lower temperatures (Fig. 4G). Altogether, these results highlight a novel mechanoresponsive mechanism built into haloarchaea, with cells orchestrating membrane fluidity and development progression to prevent premature or late cellularization.

Actin and N-glycosylation are fiducial markers for archaeal tissue polarity

Next, we searched for developmental factors specific to multicellular lifestyle by performing RNA-seq on each developmental stage (Fig. 5A). Gene expression profiles revealed that coenocytes repress twice as many as upregulated genes, possibly involving pathways related to stress response and cell division arrest (Fig. S9A). Curiously, although the number of differentially expressed genes (~28% of the genome) are distributed equally across the genome (Fig. S9B),

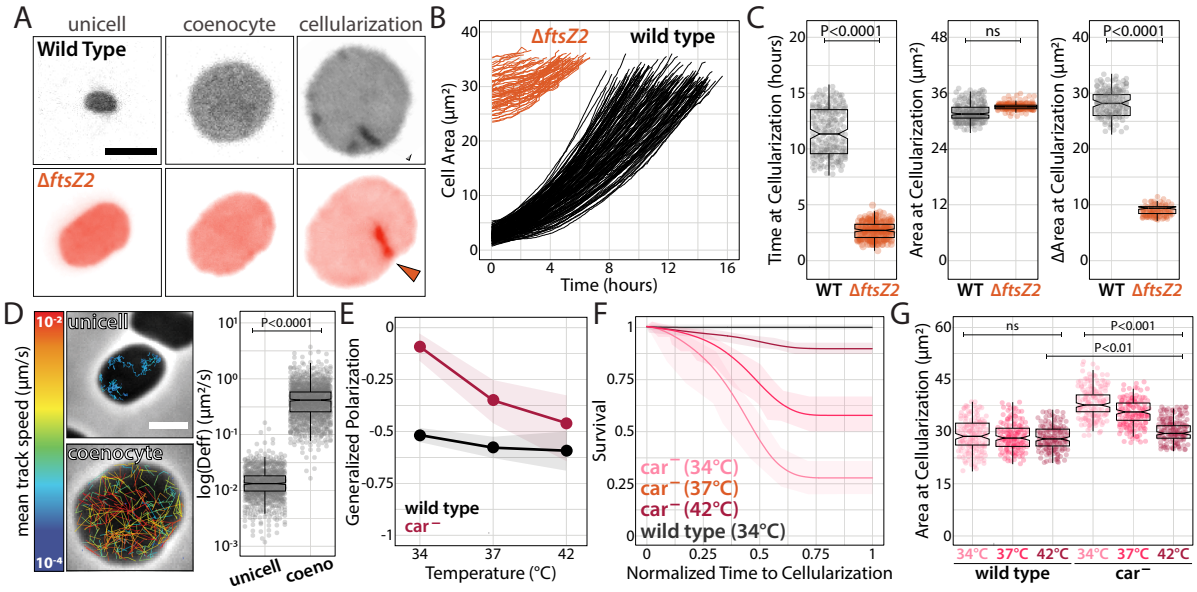

Fig. 4. Tissue cellularization is triggered by coenocytic size through a membrane tension threshold. (A) Representative epifluorescence microscopy time-lapses of wild-type (top) and Δ*ftsZ2* cells (bottom) from compression to cellularization onset **(B)** Single-cell tracking curves of cell area growth from compression to the onset of cellulation. **(C)** Time, cell area, and cell area added at the onset of cellularization. **(D)** Live-cell Generalized Polarization measurements of wild-type and car⁻ stained with Laurdan. **(E)** Normalized survival rates of wild-type (34°C) and car⁻ cells across different temperatures until cellularization. Survival was determined by cell lysis measured from phase-contrast time-lapses. **(F)** Area at cellularization measurements of wild-type and car⁻ cells across different temperatures. **(G)** (left) Phase-contrast images of unicell and coenocytes (6 hours after compression) overlayed with bSpoJ single-molecule tracks false-colored relative to their mean speed. (right) Effective diffusion coefficients calculated from Mean Square Displacement curves. The center of the boxplots indicate the median, and the limits of the box define the interquartile range; error bars represent 95% confidence interval (CI). S-layers were stained with Brilliant Blue. Statistical differences were tested by Kolmogorov-Smirnov. Unless specified, scale bars represent 2 µm.

we observed significant enrichment in the expression of genes located in the third quarter of the genome in tissues, suggesting the existence of possible multicellular gene islands (Fig. S9C). From hundreds of candidate genes, we focused on four main classes: cell surface biogenesis, cytoskeleton and mechanosensing, signaling, and cell cycle (Data S2).

Given the importance of actin in eukaryotic tissue biogenesis, we investigated the role of volactin (volA), the only identified actin homolog in *Hvo* (*39*), which was upregulated during cellularization and tissues in our RNA-seq datasets. Time-lapses of developing cells showed increased volA-msfGFP signal, consistent with our RNA-seq dataset, reaching a steady-state at the end of cellularization (Fig. 5B; Movie S12). In contrast, trapped unicells showed unaltered volA-msfGFP expression, as did tissues expressing cytoplasmic msfGFP. Moreover, volactin polymers were less abundant but highly dynamic in uncompressed apical cells compared to unicells and basal scutoids (Fig. 5C; Movie S13). Notably, cells displayed different volA spatiotemporal patterns during development, with volactin cables aligned in parallel in coenocytes and apical cells within tissues (Fig. 5D; Movie S14). Compression of Δ*volA* cells resulted in shorter coenocytes than wild type (Fig. 5E) and delayed or stalled tissue maturation (Fig. 5F). VolA and other factors have recently been implicated in regulating the development of rod-shaped (motile) and disk-shaped (sessile) cell types (*39*, *40*). Therefore, based on cellular localization, dynamics, and morphological phenotypes, we propose that volactin may mirror eukaryotic actin's multifunctional roles as a mechanosensing cytoskeleton and polarity factor in tissues (*41*).

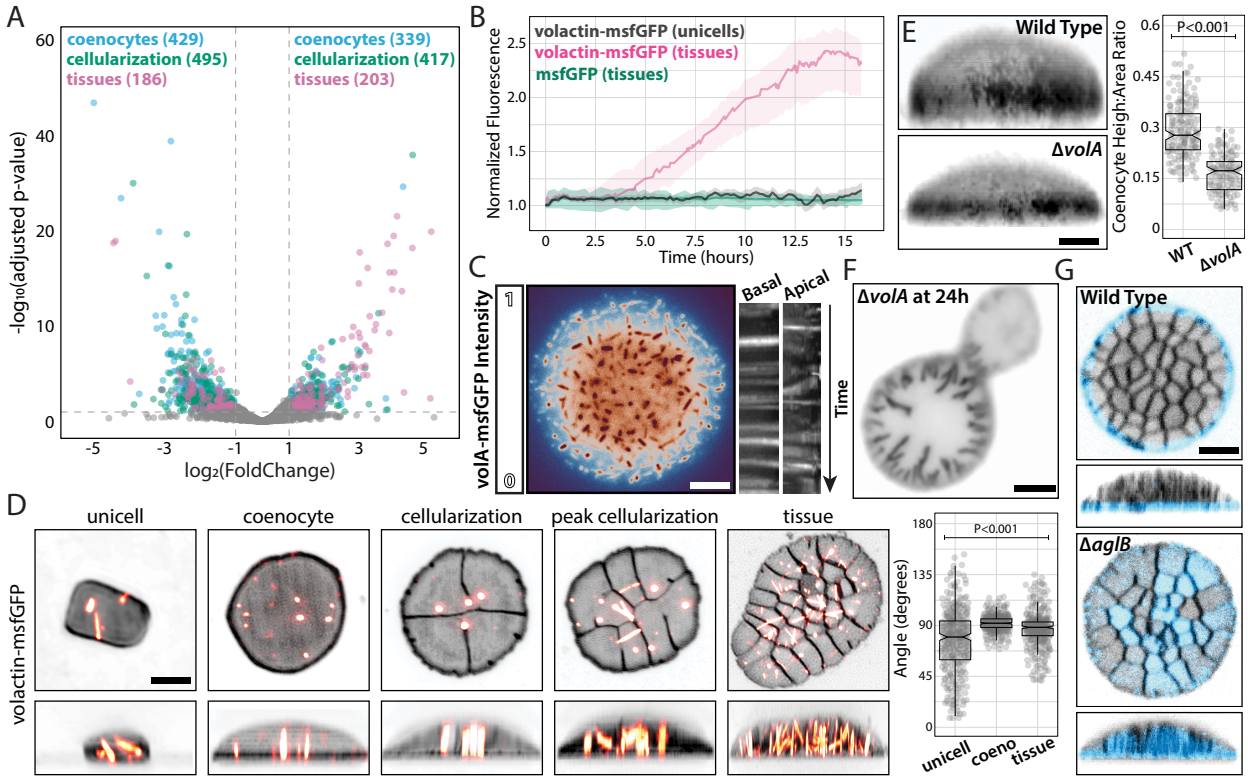

Fig. 5. Volactin and N-glycosylation are tissue-specific polarity markers. (A) Volcano plot overlays from RNA-seq datasets collected across developmental stages and normalized by liquid unicellular cultures. Parentheses indicate the number of candidates above the arbitrary cutoff. **(B)** Normalized fluorescence by cell area of volA-msfGFP and constitutively expressed cytoplasmic msfGFP from confocal time-lapses. **(C)** False-colored relative to volA-msfGFP fluorescence (left) and dynamics of volA-msfGFP polymers (right) in apical and basal area regions by epifluorescence microscopy. Kymographs were obtained across multiple cells. **(D)** 3D-SoRa microscopy of representative cells expressing volA-msfGFP across different developmental stages and quantifying volA-msfGFP cable angles within individual cells relative to the coverslip plane. **(E)** height measurements of wild-type and Δ*volA* coenocytes by 3D-SoRa microscopy. **(F)** A Δ*volA* cell stalled at cellularization. **(G)** Confocal 3D projections of cell surface N-glycosylated proteins in wild-type (top) and Δ*aglB* (bottom) tissues stained by ConA-Alexa488. The center of the boxplots indicate the median, and the box limits define the interquartile range; error bars represent a 95% confidence interval (CI). Shaded areas indicate the 95% CI. S-layers were stained with Brilliant Blue. Kolmogorov-Smirnov tested statistical differences. Unless specified, scale bars represent 2 µm.

Leveraging the differences in tissue formation across *Hfx* species (Fig. 2A), we used comparative genomics and over-representation analysis to create datasets contrasting the presence and absence of orthologous protein groups (orthogroups) among (i) *Hvo* and *Hmed* (Fig. S9D; Data S3); (ii) 4 *Hfx* species (Fig. S9E; Data S4); and (iii) orthogroups enriched in species that form tissues (Data S5). We found a strong representation of orthogroups related to protein glycosylation, sugar metabolism, and transport in all three datasets. Protein glycosylation has historically been a well-studied area in haloarchaea due to its role in mating and envelope biogenesis (*42*). N-glycosylation is also crucial for cell identity, polarity, junctions, and adhesion in multicellular eukaryotes (*43–45*). To explore the role of N-glycosylation, we labeled cells with ConA-Alexa488, a fluorescent lectin conjugate impermeable to cells, which has an affinity for various mannose glycol groups. While ConA-Alexa488 did not bind to unicellular colonies or cells in liquid cultures (Fig. S10), it exhibited a radial, halo-like localization at the periphery of apical cells in tissues (Fig. 5G; Movie S15). To test whether these radial patterns are formed by secreted proteins to the extracellular matrix space, we examined Δ*pibD* mutant that cannot process and secrete pili-dependent extracellular proteins, preventing cell adhesion to surfaces (*46*). We observed no differences on ConA-Alexa488 localization or tissue structure in Δ*pibD* tissues, suggesting that surface-adhesion-dependent biofilm is not critical for cell junctions and that ConA-Alexa488 patterns represent cell-type specific glycosylation connected to the outer surface of apical cells. To further test this idea, we imaged tissues of different N-glycosylation mutants, with Δ*aglB* being the only strain to show a disruption in ConA-Alexa488 localization, resulting in binding to both apical and basal surfaces of tissues (Fig. 5G and Fig. S10). Therefore, we propose that AglB, required for S-layer N-glycosylation (*42*), mediates tissue cell-surface polarity. This discovery adds another function to S-layer glycoproteins beyond morphogenesis and mating, establishing their role in tissue polarity.

Our discovery of clonal, tissue-like multicellularity in archaea highlights the potential of archaeal mechanobiology to shed light on the emergence of complexity in nature. Notably, this is not the first developmental program identified in haloarchaea, joining the rod-shaped (motile) and disk-shaped (sessile) shape-shift transitions (*40*). These cell types are connected by volactin, which is also required for disk formation (*39*). The coordinated alignment of volactin cables indicates that actin cables might sense membrane tension, curvature, or mechanically supporting coenocytes and basal cells (*47*). While these scenarios are not mutually exclusive, volA functions in different developmental programs can address a longstanding gap between monofunctional prokaryotic and multifunctional eukaryotic cytoskeletal polymers (*41*, *48*). Moreover, the developmental defects observed in Δ*ftsZ1-2* tissues underscore the transition from tubulin-dependent cellularization in unicellular prokaryotes to actin-dependent in eukaryotes.

Integrating biophysics and evo-devo (phys-evo-devo) offers a new framework for understanding microbial biofilms and membrane homeostasis, which regulate the transition between different (often contradictory) types of multicellularity. Evolutionarily, our data suggest the need to reinterpret past evidence for the origin of eukaryotic multicellularity, such as fossils identified as holozoans (*49*). Based on their size, shape, and lack of evident eukaryotic features, these fossils may represent ancestors of archaeal tissues. Future studies should aim to uncover the biochemical nature of cell-cell junctions and explore the presence of archaeal tissues in other phyla, particularly those closer to eukaryotes, like Asgard archaea.

References

1. S. Datta, W. C. Ratcliff, Illuminating a new path to multicellularity. *Elife* **11**, e83296 (2022).
2. M. D. Herron, J. M. Borin, J. C. Boswell, J. Walker, I.-C. K. Chen, C. A. Knox, M. Boyd, F. Rosenzweig, W. C. Ratcliff, *De novo* origins of multicellularity in response to predation. *Sci. Rep.* **9**, 2328 (2019).
3. S. Jacobeen, J. T. Pentz, E. C. Graba, C. G. Brandys, W. C. Ratcliff, P. J. Yunker, Cellular packing, mechanical stress and the evolution of multicellularity. *Nat. Phys.* **14**, 286–290 (2018).
4. T. Brunet, M. Albert, W. Roman, M. C. Coyle, D. C. Spitzer, N. King, A flagellate-to-amoeboid switch in the closest living relatives of animals. *Elife* **10** (2021).
5. O. Dudin, S. Wielgoss, A. M. New, I. Ruiz-Trillo, Regulation of sedimentation rate shapes the evolution of multicellularity in a close

unicellular relative of animals. *PLoS Biol.* **20**, e3001551 (2022).

6. B. Baum, A. Spang, On the origin of the nucleus: a hypothesis. *Microbiol. Mol. Biol. Rev.* **87**, e0018621 (2023).

7. T. A. M. Bharat, A. von Kügelgen, V. Alva, Molecular logic of prokaryotic surface layer structures. *Trends Microbiol.* **29**, 405–415 (2021).

8. M. F. Abdul-Halim, S. Schulze, A. DiLucido, F. Pfeiffer, A. W. Bisson Filho, M. Pohlschroder, Lipid Anchoring of Archaeosortase Substrates and Midcell Growth in Haloarchaea. *MBio* **11**, 10.1128/mbio.00349-20 (2020).

9. D. Moi, S. Nishio, X. Li, C. Valansi, M. Langleib, N. G. Brukman, K. Flyak, C. Dessimoz, D. de Sanctis, K. Tunyasuvunakool, J. Jumper, M. Graña, H. Romero, P. S. Aguilar, L. Jovine, B. Podbilewicz, Discovery of archaeal fusexins homologous to eukaryotic HAP2/GCS1 gamete fusion proteins. *Nat. Commun.* **13**, 3880 (2022).

10. B. Baum, D. A. Baum, The merger that made us. *BMC Biol.* **18**, 72 (2020).

11. M. Pohlschroder, S. Schulze, Haloferax volcanii. *Trends Microbiol.* **27**, 86–87 (2019).

12. K. P. Menard, N. Menard, *Dynamic Mechanical Analysis* (CRC Press, London, England, ed. 3, 2020.

13. J.-P. Rieu, H. Delanoë-Ayari, S. Takagi, Y. Tanaka, T. Nakagaki, Periodic traction in migrating large amoeba of *Physarum polycephalum*. *J. R. Soc. Interface* **12**, 20150099 (2015).

14. J. Lee, K. Jha, C. E. Harper, W. Zhang, M. Ramsukh, N. Bouklas, T. Dörr, P. Chen, C. J. Hernandez, Determining the Young's modulus of the bacterial cell envelope. *ACS Biomater. Sci. Eng.* **10**, 2956–2966 (2024).

15. C. M. Chibani, A. Mahnert, G. Borrel, A. Almeida, A. Werner, J.-F. Brugère, S. Gribaldo, R. D. Finn, R. A. Schmitz, C. Moissl-Eichinger, A catalogue of 1,167 genomes from the human gut archaeome. *Nat. Microbiol.* **7**, 48–61 (2022).

16. C. F. Guimarães, L. Gasperini, A. P. Marques, R. L. Reis, The stiffness of living tissues and its implications for tissue engineering. *Nat. Rev. Mater.* **5**, 351–370 (2020).

17. S. Shad, N. Razaghi, D. Zivar, S. Mellat, Mechanical behavior of salt rocks: A geomechanical model. *Petroleum* **9**, 508–525 (2022).

18. E. Kalinka, S. M. Brody, A. J. M. Swafford, E. M. Medina, L. K. Fritz-Laylin, Genetic transformation of the frog-killing chytrid fungus *Batrachochytrium dendrobatidis*. *Proc. Natl. Acad. Sci. U. S. A.* **121**, e2317928121 (2024).

19. Y. S. Hwang, M. Seo, H. J. Choi, S. K. Kim, H. Kim, J. Y. Han, The first whole transcriptomic exploration of pre-oviposited early chicken embryos using single and bulked embryonic RNA-sequencing. *Gigascience* **7**, 1–9 (2018).

20. O. Hamant, E. S. Haswell, Life behind the wall: sensing mechanical cues in plants. *BMC Biol.* **15**, 59 (2017).

21. C. Villeneuve, A. Hashmi, I. Ylivinkka, E. Lawson-Keister, Y. A. Miroshnikova, C. Pérez-González, S.-M. Myllymäki, F. Bertillot, B. Yadav, T. Zhang, D. Matic Vignjevic, M. L. Mikkola, M. L. Manning, S. A. Wickström, Mechanical forces across compartments coordinate cell shape and fate transitions to generate tissue architecture. *Nat. Cell Biol.* **26**, 207–218 (2024).

22. D. Kuipers, A. Mehonic, M. Kajita, L. Peter, Y. Fujita, T. Duke, G. Charras, J. E. Gale, Epithelial repair is a two-stage process driven first by dying cells and then by their neighbours. *J. Cell Sci.* **127**, 1229–1241 (2014).

23. W. Kong, O. Loison, P. Chavadimane Shivakumar, E. H. Chan, M. Saadaoui, C. Collinet, P.-F. Lenne, R. Clément, Experimental validation of force inference in epithelia from cell to tissue scale. *Sci. Rep.* **9**, 14647 (2019).

24. L. E. Mayerhofer, A. J. Macario, E. Conway de Macario, Lamina, a novel multicellular form of *Methanosarcina mazei* S-6. *J. Bacteriol.* **174**, 309–314 (1992).

25. N. Wadhwa, H. C. Berg, Bacterial motility: machinery and mechanisms. *Nat. Rev. Microbiol.* **20**, 161–173 (2022).

26. A. Oren, Why isn't *Haloferax mediterranei* more "weed-like"? *FEMS Microbiol. Lett.* **364** (2017).

27. S. Kim, M. Pochitaloff, G. A. Stooke-Vaughan, O. Campàs, Embryonic tissues as active foams. *Nat. Phys.* **17**, 859–866 (2021).

28. E. P. Bingham, W. C. Ratcliff, A nonadaptive explanation for macroevolutionary patterns in

the evolution of complex multicellularity. *Proc. Natl. Acad. Sci. U. S. A.* **121**, e2319840121 (2024).

29. B. E. Shapiro, H. Jonsson, P. Sahlin, M. Heisler, A. Roeder, M. Burl, E. M. Meyerowitz, E. D. Mjolsness, Tessellations and pattern formation in plant growth and development, *arXiv [q-bio.CB]* (2012). http://arxiv.org/abs/1209.2937.

30. P. Gómez-Gálvez, P. Vicente-Munuera, A. Tagua, C. Forja, A. M. Castro, M. Letrán, A. Valencia-Expósito, C. Grima, M. Bermúdez-Gallardo, Ó. Serrano-Pérez-Higueras, F. Cavodeassi, S. Sotillos, M. D. Martín-Bermudo, A. Márquez, J. Buceta, L. M. Escudero, Scutoids are a geometrical solution to three-dimensional packing of epithelia. *Nat. Commun.* **9**, 2960 (2018).

31. B. I. Shraiman, Mechanical feedback as a possible regulator of tissue growth. *Proc. Natl. Acad. Sci. U. S. A.* **102**, 3318–3323 (2005).

32. S. Ithurbide, S. Gribaldo, S.-V. Albers, N. Pende, Spotlight on FtsZ-based cell division in Archaea. *Trends Microbiol.*, doi: 10.1016/j.tim.2022.01.005 (2022).

33. O. Dudin, A. Ondracka, X. Grau-Bové, A. A. Haraldsen, A. Toyoda, H. Suga, J. Bråte, I. Ruiz-Trillo, A unicellular relative of animals generates a layer of polarized cells by actomyosin-dependent cellularization. *Elife* **8** (2019).

34. N. Fraikin, A. Couturier, C. Lesterlin, A palette of bright and photostable monomeric fluorescent proteins for bacterial time-lapse imaging, *bioRxiv* (2024)p. 2024.03.28.587235.

35. M. Olivetta, O. Dudin, The nuclear-to-cytoplasmic ratio drives cellularization in the close animal relative *Sphaeroforma arctica*. *Curr. Biol.* **33**, 1597-1605.e3 (2023).

36. A. Ondracka, O. Dudin, I. Ruiz-Trillo, Decoupling of Nuclear Division Cycles and Cell Size during the Coenocytic Growth of the Ichthyosporean *Sphaeroforma arctica*. *Curr. Biol.* **28**, 1964-1969.e2 (2018).

37. W. Seel, D. Baust, D. Sons, M. Albers, L. Etzbach, J. Fuss, A. Lipski, Carotenoids are used as regulators for membrane fluidity by *Staphylococcus xylosus*. *Sci. Rep.* **10**, 330 (2020).

38. S. A. Sanchez, M. A. Tricerri, E. Gratton, Laurdan generalized polarization fluctuations measures membrane packing micro-heterogeneity *in vivo*. *Proc. Natl. Acad. Sci. U. S. A.* **109**, 7314–7319 (2012).

39. H. Schiller, J. Kouassi, Y. Hong, T. Rados, J. Kwak, A. DiLucido, D. Safer, A. Marchfelder, F. Pfeiffer, A. Bisson-Filho, S. Schulze, M. Pohlschroder, Identification and characterization of structural and regulatory cell-shape determinants in *Haloferax volcanii*, *bioRxiv* (2023).https://doi.org/10.1101/2023.03.05.531186.

40. Z. Curtis, P. Escudeiro, J. Mallon, O. Leland, T. Rados, A. Dodge, K. Andre, J. Kwak, K. Yun, B. Isaac, M. Martinez Pastor, A. K. Schmid, M. Pohlschroder, V. Alva, A. Bisson, Halofilins as emerging bactofilin families of archaeal cell shape plasticity orchestrators. *Proc. Natl. Acad. Sci. U. S. A.* **121**, e2401583121 (2024).

41. A. Charles-Orszag, N. A. Petek-Seoane, R. D. Mullins, Archaeal actins and the origin of a multi-functional cytoskeleton. *J. Bacteriol.* **206**, e0034823 (2024).

42. S. Schulze, F. Pfeiffer, B. A. Garcia, M. Pohlschroder, Comprehensive glycoproteomics shines new light on the complexity and extent of glycosylation in archaea. *PLoS Biol.* **19**, e3001277 (2021).

43. O. Vagin, J. A. Kraut, G. Sachs, Role of N-glycosylation in trafficking of apical membrane proteins in epithelia. *Am. J. Physiol. Renal Physiol.* **296**, F459-69 (2009).

44. A. Liwosz, T. Lei, M. A. Kukuruzinska, N-glycosylation affects the molecular organization and stability of E-cadherin junctions. *J. Biol. Chem.* **281**, 23138–23149 (2006).

45. T. Brunet, D. S. Booth, Cell polarity in the protist-to-animal transition. *Curr. Top. Dev. Biol.* **154**, 1–36 (2023).

46. R. N. Esquivel, S. Schulze, R. Xu, M. Hippler, M. Pohlschroder, Identification of Haloferax volcanii pilin N-glycans with diverse roles in pilus biosynthesis, adhesion, and microcolony formation. *J. Biol. Chem.* **291**, 10602–10614 (2016).

47. P. Lappalainen, T. Kotila, A. Jégou, G. Romet-Lemonne, Biochemical and mechanical regulation of actin dynamics. *Nat. Rev. Mol. Cell Biol.* **23**, 836–852 (2022).

48. J. A. Theriot, Why are bacteria different from eukaryotes? *BMC Biol.* **11**, 119 (2013).

49. P. K. Strother, M. D. Brasier, D. Wacey, L. Timpe, M. Saunders, C. H. Wellman, A possible billion-year-old holozoan with differentiated multicellularity. *Curr. Biol.* **31**, 2658-2665.e2 (2021).

Acknowledgments

The Bisson Lab appreciates Bruce Goode (Brandeis U) for access to the SoRa microscope, and also Avital Rodal (Brandeis U), Buzz Baum (MRC-LMB), and Harold Erickson (Duke U) for constructive suggestions on the manuscript. STED and spectral confocal microscopy were performed at the Brandeis Light Microscopy Core Facility. We want to thank Steven Bruckbauer for the chromosomal mNeonGreen-PCNA strain. TR would like to thank the MBL Woods Hole Physiology Course and Biovis for iSIM use. We are grateful to the Scientific Community Image Forum and the Center for Open Bioimage Analysis (COBA) for fostering an invaluable intellectual community dedicated to training microscopists in image analysis. We acknowledge the MRC LMB electron microscopy facility for sample preparation and data collection. This work was supported by the NIH grant 1S10OD034223-01 for the Abberior Facility Line STED microscope, housed in the Brandeis Light Microscopy Core Facility; Moore–Simons Project on the Origin of the Eukaryotic Cell (doi:10.46714/735929LPI) awarded to AB; the Human Frontiers Science Program (RGY0074/2021) awarded to AB, TAMB, and VA; the NSF Grant (NSF-MBC2222076) awarded to AB; and the Brandeis National Science Foundation (NSF) Materials Research Science and Engineering Center (MRSEC) Bioinspired Soft Materials (NSF-DMR 2011846). AB is a Pew Scholar in the Biomedical Sciences, supported by The Pew Charitable Trusts. This work was supported by the Medical Research Council, as part of United Kingdom Research and Innovation (also known as UK Research and Innovation) [Programme MC_UP_1201/31 to TAMB]. TAMB would like to thank the European Molecular Biology Organization, the Wellcome Trust (Grant 225317/Z/22/Z) and the Leverhulme Trust. IC was supported by an EMBO Long-Term Fellowship (ALTF 92-2022). This work was partly supported by institutional funds of the Max Planck Society. VA would like to thank Andrei Lupas (MPI Tübingen) for their continued support.

Author contributions

Conceptualization: TR, OL, AB
Methodology: TR, OL, PE, JM, KA, ES, SN, IP, LTR, LR, YS, AB
Investigation: TR, OL, PE, JM, KA, IC, AvK, SN, LTR, TAMB, AB
Visualization: TR, OL, PE, KA, AB
Funding acquisition: AB, VA, TAMB, VT
Project administration: AB
Supervision: TR, SK, YS, TAMB, VA, AB
Writing – original draft: TR, OL, AB
Writing – review & editing: TR, OL, PE, JM, KA, IC, AvK, ES, SN, IP, SK, LR, VT, YS, TAMB, VA, AB Conceptualization: SBB, DLA, MPW

Competing interests

Authors declare that they have no competing interests.

Data and materials availability

All custom software used in this work is publicly available without restrictions at https://github.com/Archaea-Lab/Multicell_paper and other repositories described in the Supporting Materials. The complete raw RNA-seq datasets presented in this study can be found in NCBI GEO online repository PRJNA1165275.

Supplementary Materials

Materials and Methods
Figs. S1 to S10
Tables S1 to S6
References (50–140)
Movies S1 to S15

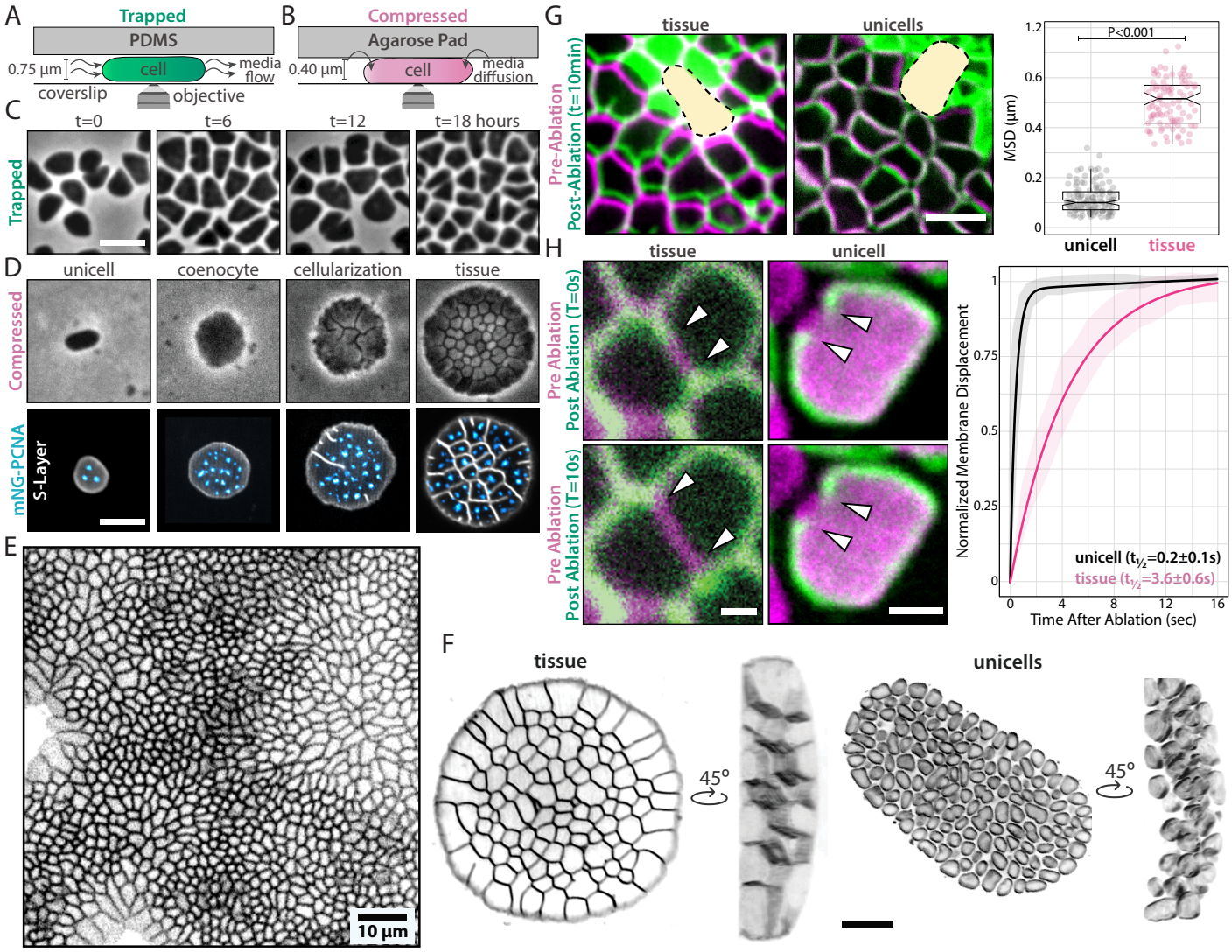
A
Trapped
PDMS
0.75 µm
cell
media flow
coverslip
objective
B
Compressed
Agarose Pad
0.40 µm
cell
media diffusion
C
t=0
t=6
t=12
t=18 hours
Trapped
D
unicell
coenocyte
cellularization
tissue
Compressed
mNG-PCNA
S-Layer
E
10 µm
F
tissue
45°
unicells
45°
G
tissue
unicells
Pre-Ablation
Post-Ablation (t=10min)
P<0.001
MSD (µm)
unicell
tissue
H
tissue
unicell
Pre Ablation
Post Ablation (T=0s)
Pre Ablation
Post Ablation (T=10s)
Normalized Membrane Displacement
unicell (t½=0.2±0.1s)
tissue (t½=3.6±0.6s)
Time After Ablation (sec)

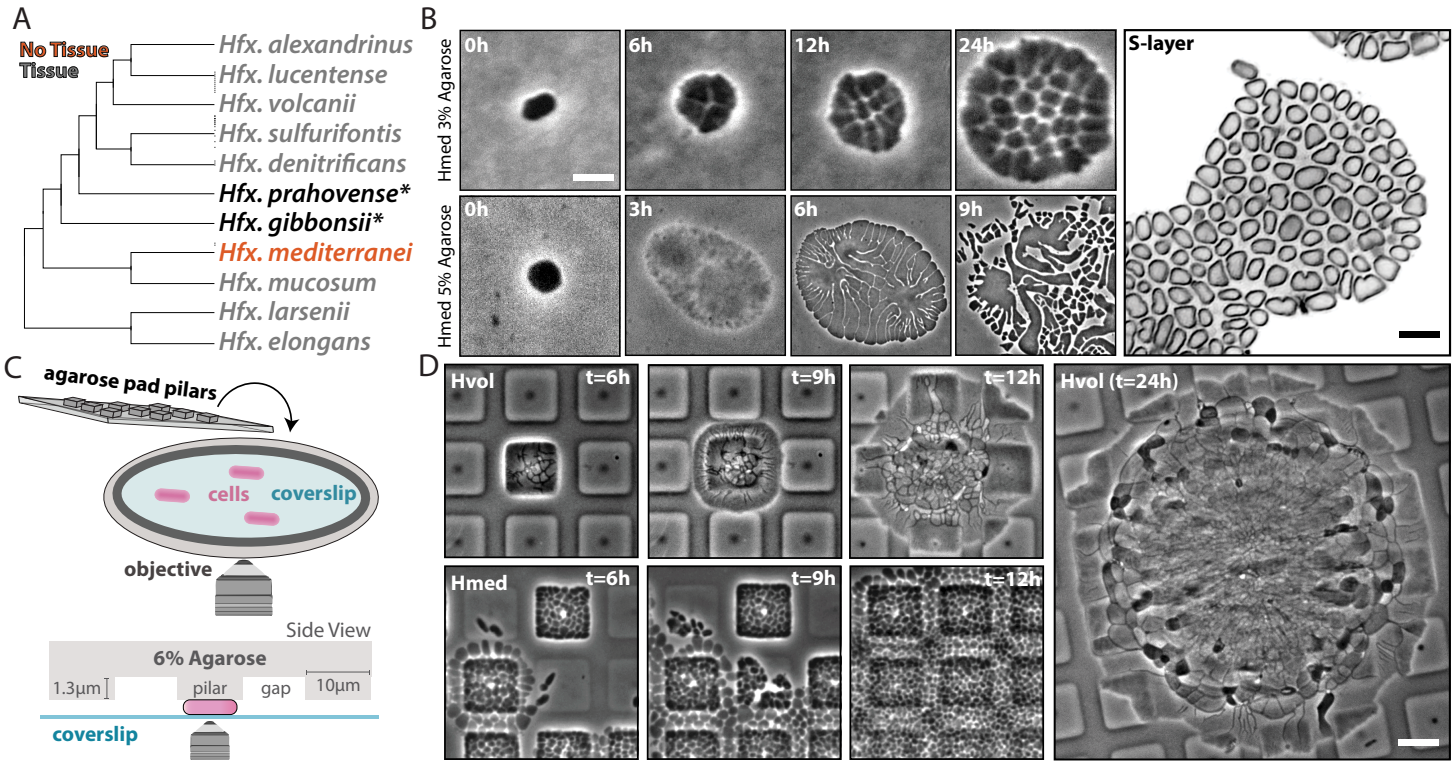
A
No Tissue
Tissue
Hfx. alexandrinus
Hfx. lucentense
Hfx. volcanii
Hfx. sulfurifontis
Hfx. denitrificans
Hfx. prahovense*
Hfx. gibbonsii*
Hfx. mediterranei
Hfx. mucosum
Hfx. larsenii
Hfx. elongans
B
Hmed 3% Agarose
0h
6h
12h
24h
Hmed 5% Agarose
0h
3h
6h
9h
S-layer
C
agarose pad pilars
cells
coverslip
objective
Side View
6% Agarose
1.3µm
pilar
gap
10µm
coverslip
D
Hvol
t=6h
t=9h
t=12h
Hvol (t=24h)
Hmed
t=6h
t=9h
t=12h

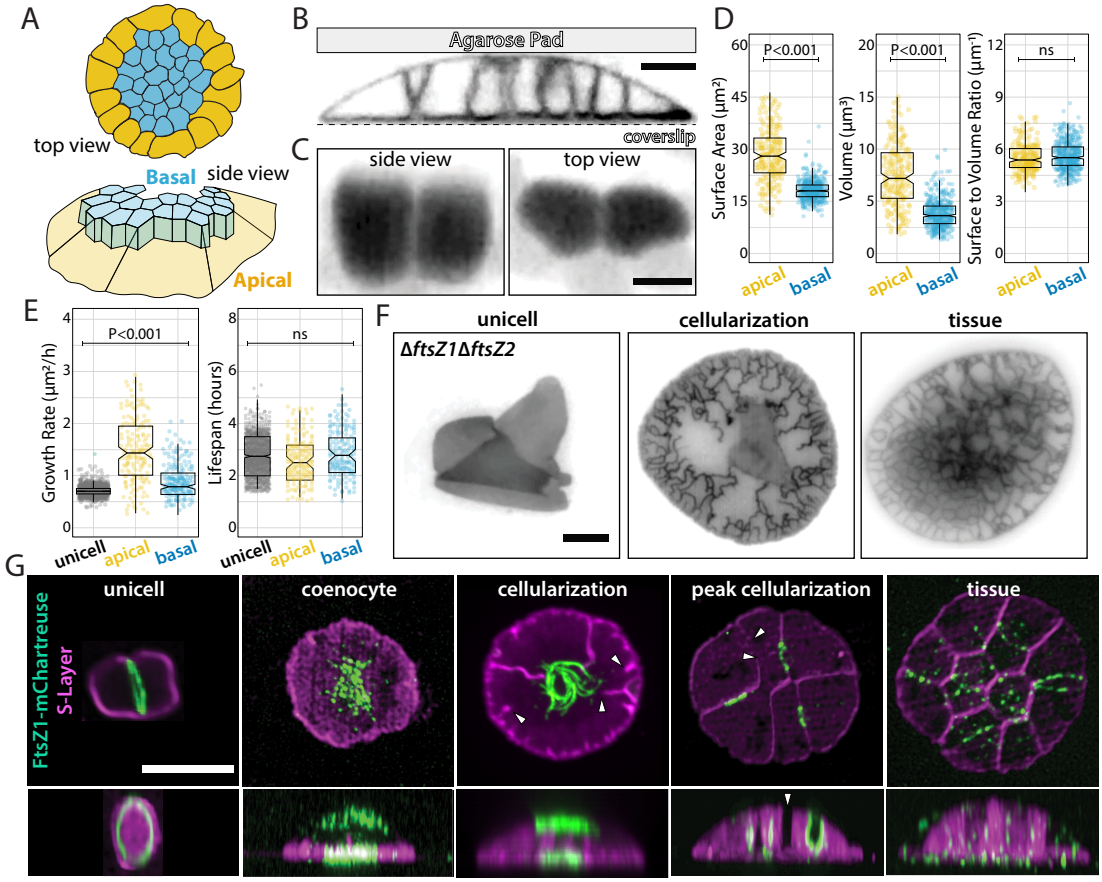
A
top view
Basal
side view
Apical
B
Agarose Pad
coverslip
C
side view
top view
D
P<0.001
Surface Area (µm²)
P<0.001
Volume (µm³)
ns
Surface to Volume Ratio (µm⁻¹)
apical
basal
E
P<0.001
Growth Rate (µm²/h)
ns
Lifespan (hours)
unicell
apical
basal
F
unicell
cellularization
tissue
ΔftsZ1ΔftsZ2
G
unicell
coenocyte
cellularization
peak cellularization
tissue
FtsZ1-mChartreuse
S-Layer

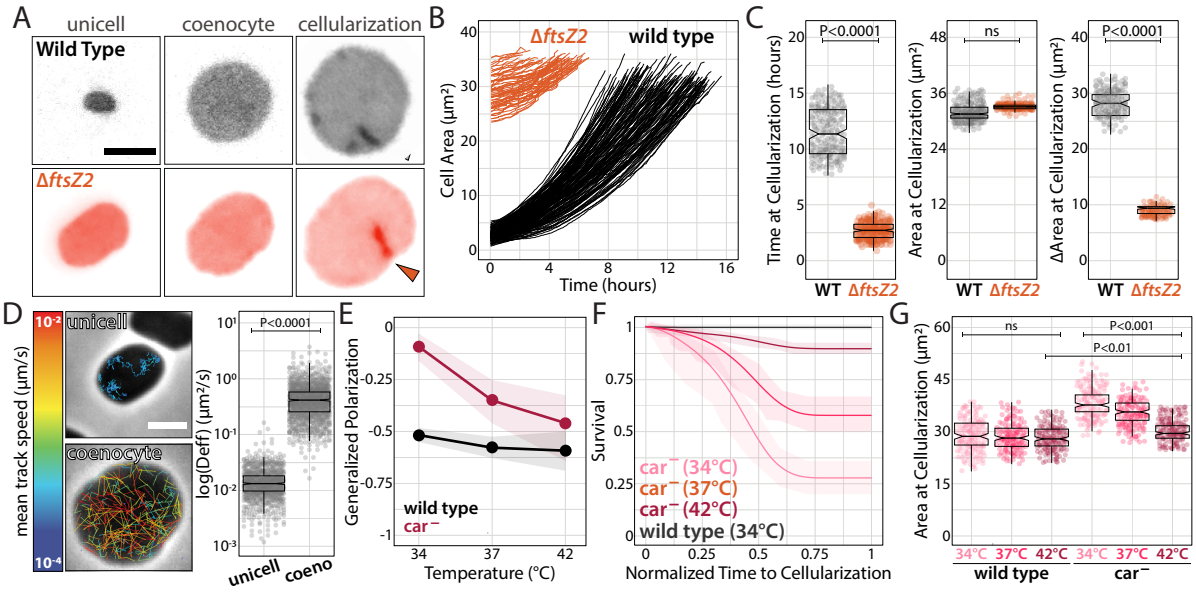
A
unicell
coenocyte
cellularization
Wild Type
ΔftsZ2
B
ΔftsZ2
wild type
Cell Area (µm²)
Time (hours)
C
P<0.0001
Time at Cellularization (hours)
ns
Area at Cellularization (µm²)
P<0.0001
ΔArea at Cellularization (µm²)
WT
ΔftsZ2
D
unicell
coenocyte
mean track speed (µm/s)
log(Deff) (µm²/s)
P<0.0001
unicell
coeno
E
Generalized Polarization
wild type
car⁻
Temperature (°C)
F
Survival
car⁻ (34°C)
car⁻ (37°C)
car⁻ (42°C)
wild type (34°C)
Normalized Time to Cellularization
G
ns
P<0.001
P<0.01
Area at Cellularization (µm²)
34°C
37°C
42°C
wild type
car⁻

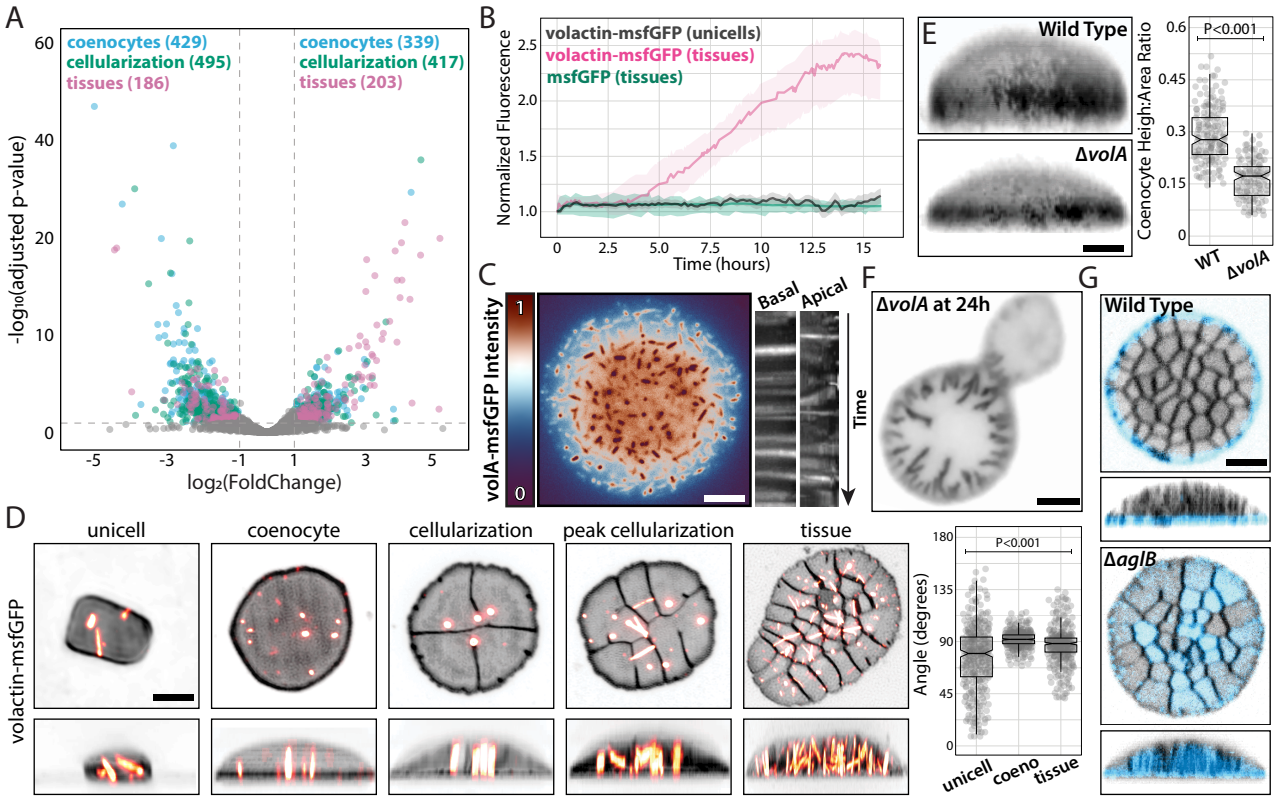
A
coenocytes (429)
cellularization (495)
tissues (186)
coenocytes (339)
cellularization (417)
tissues (203)
-log10(adjusted p-value)
log2(FoldChange)
B
volactin-msfGFP (unicells)
volactin-msfGFP (tissues)
msfGFP (tissues)
Normalized Fluorescence
Time (hours)
E
Wild Type
ΔvolA
Coenocyte Heigh:Area Ratio
P<0.001
WT
ΔvolA
C
volA-msfGFP Intensity
Basal
Apical
Time
F
ΔvolA at 24h
G
Wild Type
ΔaglB
Angle (degrees)
P<0.001
unicell
coeno
tissue
D
unicell
coenocyte
cellularization
peak cellularization
tissue
volactin-msfGFP